Unconventional filling dynamics of a pit crater

(Article begins on next page)

16 October 2023

1   # Unconventional filling dynamics of a pit crater

2   **P.-Y. Burgi[1*], S. Valade[2], D. Coppola[3], G. Boudoire[4,], G. Mavonga[5], F. Rufino[6], and D. Tedesco[6,7,8,9]**

3

4   [1] IT Department, University of Geneva, 1211 Genève, Switzerland.

5   [2] Departamento de Vulcanología, Instituto de Geofísica, Universidad Nacional Autónoma de
6   México, Mexico City, Mexico.

7   [3] Dipartimento di Scienze della Terra, Università di Torino, Torino, Italia.

8   [4] Laboratoire Magmas et Volcans, UCA, CNRS, IRD, OPGC, 63178 Aubière, France.

9   [5] Observatoire Volcanologique de Goma, Goma, RDC.

10   [6] Università degli Studi della Campania "Luigi Vanvitelli", DiSTABIF, 81100 Caserta, Italia.

11   [7] Istituto Nazionale Geofisica e Vulcanologia, Osservatorio Vesuviano, Via Diocleziano, Napoli,
12   Italia.

13   [8] European Union Delegation, Kinshasa, DRC – Bruxelles, European Union.

14   [9] MONUSCO (United Nations)- Goma, Democratic Republic of Congo.

15   * Corresponding author Pierre-Yves Burgi (pierre-yves.burgi@unige.ch)

16

17   **Abstract**

18   The rise and fall of magma columns is a process commonly observed in volcanoes hosting lava

19   lakes and serves as proxy of magmatic reservoir pressure and warning for potential eruptions. This

20   dynamic process typically involves the filling and emptying of a "pit crater" - a cylindrical depression

21   usually formed by one or more collapses of a structure lying above an emptied surficial reservoir.

22   Between 2016 and 2020, the 300 m deep pit crater located within Nyamulagira volcano (Democratic

23   Republic of Congo) underwent an unusual filling dynamic. In May 2019 while filled to about 90%

24   the crater floor collapsed by 90 m within two months, followed by the rapid emergence of a sub-

25 circular solidified block overlooking the crater rim in less than 6 months. Using numerical

26 simulations of models based on thermal energy and constrained by multiparametric data, we

27 account for the incremental filling of the crater by successive intra-crateric lava flows and the

28 subsequent collapse of the crater floor. We further characterize this unconventional filling mode

29 based on thermal budget considerations.

30

31 **Keywords:** volcano; remote sensing; pit crater; lava lake; thermal model, thermal budget

32

33 **1. Introduction**

34 Pit craters are common features on basaltic volcanoes (Harris, 2009), defined as cylindrical

35 depressions with steeply inward dipping sides usually formed by one or more collapses of a

36 structure lying above an associated emptied surficial reservoir. Their evolution is closely related to

37 near surface magmatic activity (Walker, 1988). Pit craters may or may not be occupied by lava

38 lakes. Those lava lakes may be active, fed from depth and usually persistent over substantial period

39 of time. Their level within the crater vary in accordance to pressure changes at the base of a

40 convecting magmatic column (Burgi et al., 2020, 2002; Coppola et al., 2016a; Duffell et al., 2003;

41 Lev et al., 2019; Patrick et al., 2019; Valade et al., 2018). Inactive lava lakes are in turn accounted

42 for by lavas erupted from active vents inside or outside the pit crater, spreading intermittent lava

43 flows within it (Harris, 2009; Swanson et al., 1979). Termination of magma supply will cause the

44 entrapped lava layers to gradually cool and solidify.

45 While the dynamic of active (convective) lava lakes have been extensively modelled (e.g., Harris,

46 2008), the emplacement of inactive lava lakes still lack a dedicated model able to explain the

47 complex dynamics of filling, emptying and solidification operating within these structures (e.g.,

48 Harris, 2009). The two filling dynamics (active and inactive), may produce similar surface structures

49 making the recognition of one mechanism rather than another not trivial. However, the two

50 mechanisms are likely characterized by different ratio between the thermal energy radiated by the

51 lake surface, and the volumetric growth rate inside the pit crater. In fact, active lava lakes radiate

52 much more thermal energy than that contained in the lava that eventually accumulates on the

53 surface (Coppola et al., 2013). This is because the convective magma column allows the hot

54 magma to rise, degas and loose heat, before most of it is cycled back into the system (Burgi et al.,

55 2020, 2002). The extreme case is visible in stable, long-lived lava lakes that emit a considerable

56 amount of heat without increasing its volume (e.g. Erta Ale, Erebus, Nyiragongo during stable

57 phases, Harris et al., 1999). On the contrary, inactive lava lakes, being basically fed by an effusive

58 activity, are characterized by thermal emissions that are proportional to the volume of erupted lava

59 (Coppola et al., 2013; Harris and Baloga, 2009), without any additional contribution due to

60 convective processes.

61 In this study we report the evolution of a new lava lake which appeared inside a summit pit crater

62 of Nyamulagira (Democratic Republic of Congo) in 2014 (Fig. 1c). Ground and satellite

63 observations (see methodology) have made it possible to track the filling dynamic of the pit crater

64 by measuring the volume of lava accumulating inside, as well as the net discharge rate (Q_{out}) and

65 the volcanic radiant power associated to the surface activity (VRP). These observations highlight

66 the occurrence of distinct phases of rise of the pit-crater floor, that cannot be accounted exclusively

67 by one of the above-mentioned models, but rather by a transition from active to inactive filling

68 mechanism. Moreover, during the phase of inactive lava lake emplacement, we observe the

69 subsidence of the pit-crater floor, followed by the uplift of a solidified basaltic block whose dynamics

70 shares typical aspects of both the subsidence and resurgence of solid blocks observed in caldera-

71 forming eruptions.

72 We thus focus on the peculiar filling-emptying-filling dynamics characterizing the inactive lava lake

73 stage between 2016 and 2020, and we propose a thermal model (fed by remote-sensed data)

74 whereby successive intra-crater lava flows pile up at different rates to produce layers of lava with

75 different states of solidification. On this basis, our model is able to explain the complex pit-crater

76 evolution recently observed at Nyamulagira which include the unusual subsidence and block uplift,

77 rarely observed at mafic calderas (Galetto et al., 2019; Geist et al., 2006a).

78 **2. Nyamulagira setting**

79 Nyamulagira is the westernmost volcano of the Virunga Volcanic Province (Democratic Republic

80 of Congo - DRC) in the western branch of the East African Rift System (EARS) (Fig. 1a). It is a

81 predominantly mafic shield volcano with a 3058-m-high summit caldera, a diameter of more than 2

82 km, and one of the most active volcanoes of the EARS (Bluth and Carn, 2008). As many basaltic

83 shield volcanoes, Nyamulagira is mostly characterized by frequent flank eruptions, with a total of

84 40 occurrences from the summit crater and from its flanks over the last 120 years (Michellier et al.,

85 2020; Pouclet and Bram, 2021). The presence of a lava lake has also been documented in 1930-

86 1938 (Wadge and Burt, 2011) and its drainage in 1938 has led to the longest (more than 2 years)

87 and most voluminous (>200 x 10^6 m^3) historical eruptive event (Pouclet, 1975; Wadge and Burt,

88 2011), with lava flows rapidly reaching Lake Kivu located 25 km downstream. The very end of the

89 2011–2012 peripheral eruption was marked by a co-eruptive explosive collapse of a pit crater floor

90 in the caldera's north-eastern sector. After a period of 74 years (R. Hoier, 1939) a new lava lake

91 was firstly observed in 2014 (Campion, 2014; Coppola et al., 2016a; Smets et al., 2015, 2014),

92 occupying the bottom of this pit crater estimated between 400 and 500 m deep. This pit crater has

93 now almost (not always) lost its frequent use as a lava lake container and seems to represent the

94 central (superficial) part of Nyamulagira's plumbing system (Pouclet and Bram, 2021; Wauthier et

95 al., 2013).
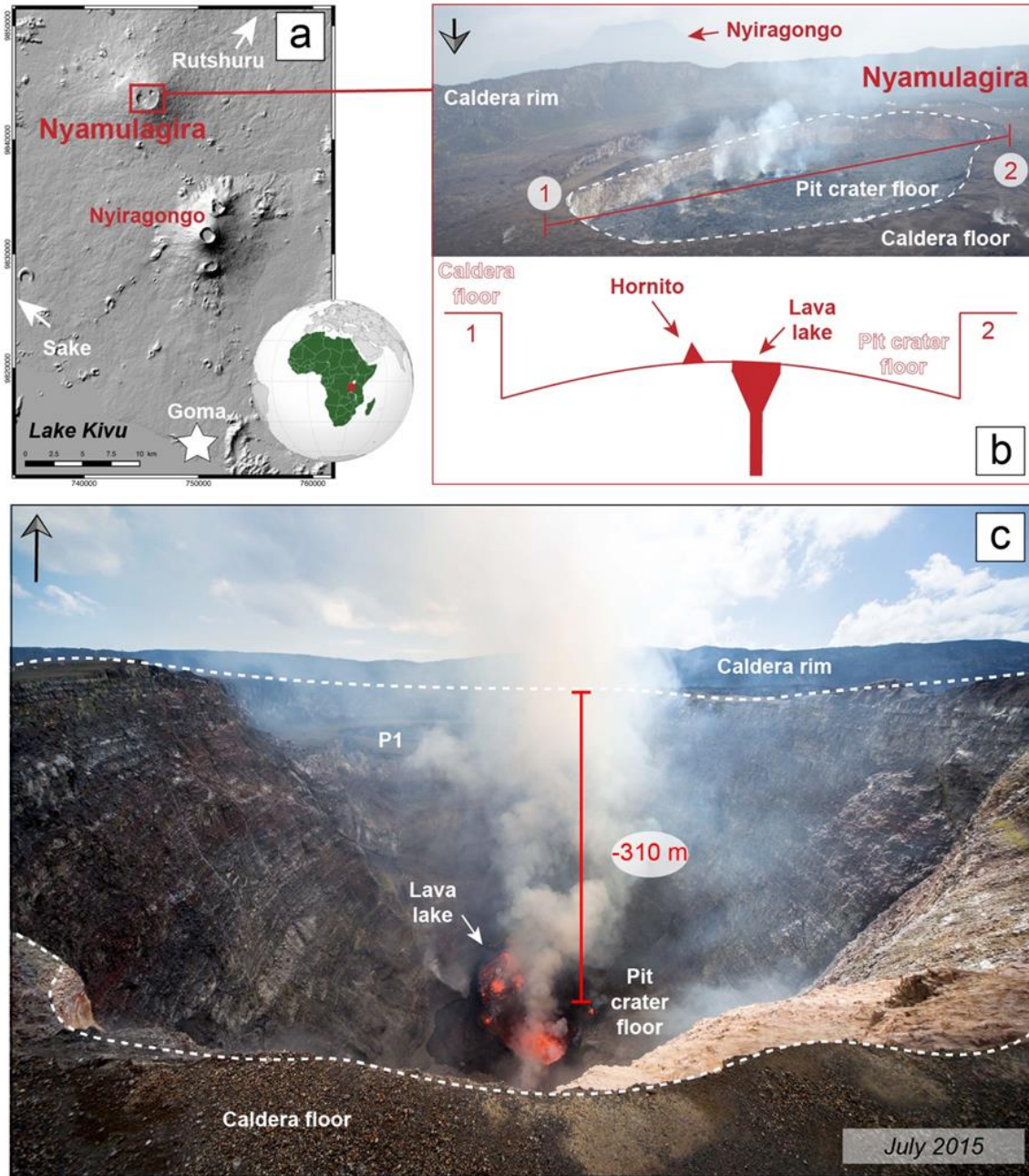
96

97   **Fig. 1.** Setting of the pit crater. (a) Location of Nyamulagira and Nyiragongo (another active
98   volcano), and the City of Goma. Digital Elevation Model (DEM) computed from the Shuttle Radar
99   Topography Mission (SRTM, 2000) data extracted from USGS Earth Explorer. (b) Aerial image on
100   February 18, 2019 pointing out the morphology of the pit crater at Nyamulagira along with cross
101   section schematically illustrated (vertical scale exaggerated). At this time the pit crater was about
102   600 m long and 400 m wide and was almost completely filled. (c) The pit crater in July 2015.
103   Pictures from the authors.
104

105   **3.   Methodology**

106   **3.1 Data Acquisition**

107   Periodic field surveys inside the Nyamulagira caldera were carried out between November 2014

108   and February 2020 with the support of the Observatoire Volcanologique de Goma (OVG) and the

109   MONUSCO (United Nations Organization Stabilization Mission in DRC). During each mission (from

110   a few hours to several days), a comprehensive series of field observations and measurements were

111   conducted to document the physical configuration of the active pit crater, using Laser Range Finder

112   Binoculars. These field campaigns were supplemented by helicopter observations performed by

113   MONUSCO whenever they could fly over this region. which made it possible to estimate the pit-

114   crater floor level at different states of its evolution with an accuracy of about 10% of the absolute

115   value.

116   These estimations were complemented by Sentinel-1 Synthetic-Aperture Radar (SAR) images

117   processed by the MOUNTS volcano monitoring system (Valade et al., 2019) ([www.mounts-](www.mounts-project.com)

118   [project.com](www.mounts-project.com)) to measure both the pit-crater depth evolution and the caldera deformation, from

119   January 2018 to June 2020. Depth is calculated from the intensity image, by measuring the length

120   of the shadow casted by the pit crater walls in radar geometry, and multiplying it by the cosine of

121   the radar incidence angle (Wadge et al., 2011). The method has successfully been applied to track

122   lava lake level variations (Barrière et al., 2018; Moore et al., 2019), and here provides continuous

123   variations of the pit-crater floor, which are validated by sporadic field measurements. Deformation

124   is calculated from standard differential SAR interferometry analysis (D-InSAR), with interferograms

125   computed with the shortest temporal baseline, i.e., between two consecutive acquisitions (typically

126   6-day interval on the ascending track, and 12-days interval on the descending track). Unwrapping

127   of the interferograms was done with SNAPHU to recover ground deformation in the radar line-of-

128   sight (LOS) in meters. The ground and satellite data relating to the depth of the pit crater were used

129   to calculate the volume of lava accumulating inside the pit crater (assuming an inverted truncated

130   cone geometry with r_{min}= 113 m and r_{max}= 250 m; Fig. 2a). Volumetric estimates have been finally

131   used to calculate growth rate (Q_{out}) for each analyzed period (Fig. 2b).

132   Thermal emissions have been detected using infrared data provided by the moderate resolution

133   imaging spectroradiometer (MODIS), compiled within the Middle InfraRed Observation of Volcanic

134   Activity (MIROVA) system (Coppola et al., 2016b; www.mirovaweb.it) to facilitate their analysis and

135   determine the volcanic radiative power (VRP; Fig. 2c). The MODIS data were supported by the

136   images acquired from the Copernicus Sentinel 2 sensors (resolution of 20 m in the short-wave

137   infrared - SWIR bands), which made it possible to identify in greater spatial detail the high

138   temperature areas at the origin of the measured heat flux.

139   **4. Observations and measurements**

140   **4.1 Pit-crater filling dynamic between 2014 and 2020**

141   First observations of a lava lake inside the summit pit-crater of Nyamulagira date back to mid-2014

142   (Coppola et al., 2016b) when visual observations confirmed the presence of fresh magma (~50 m

143   diameter) lava lake at the bottom of the pit-crater (~500 m depth). In July 2015, the lava lake

144   displayed an elliptical shape, 150 m long and 100 m wide, and was located at a depth of 310 m

145   below the crater rim (Fig. 1c). This initial phase of activity (volume less than 2 x 10^6 m^3) was followed

146   by a period without any evidence of lava lake activity (Supp. Fig. S1a) until December 2016, when

147   the pit crater started to be filled by fresh lava. The new vigorous filling phase led the pit crater floor

148   to rise at a depth of 160 m below the crater rim, with a diameter of ~190 m and a volume of

149   ~14 x 10^6 m^3 by May 2017 (Supp. Fig. S1b). A new phase of rest occurred between June 2017 and

150   May 2018 when the third filling phase started (see next section). Overall, the volume of lava

151   accumulated in the pit-crater from April 2014 to April 2020 amounts to approximately 37 x 10^6 m^3

152   with an average magma output rate of 0.18 m^3/s (Fig. 2a). This volume of lava accounts for only

153   12% of the long-term magma output rate of Nyamulagira between 1980 and 2012 (~1.5 m^3/s;

154   Coppola et al., 2016a; Fig. 2b).

155   The three main phases of lava lake growth are well highlighted by the cumulative volume trend as

156   well as by the evolution of the lava discharge rate (Q_{out}) and by the VRP (Fig. 2). As anticipated in

157   the introduction the ratio between thermal flux (VRP) and volumetric growth rate (Q_{out}), hereby

158   defined as c_{rad}= VRP/Q_{out} (Coppola et al., 2013) is a parameter representing the amount of heat

159   radiated into the atmosphere for each cubic meter of lava erupted or accumulated inside the crater

160   (Fig. 2d). c_{rad} outlines how the three phases represented in Fig. 2a, were characterized by

161   markedly different values (Fig. 2d), likely associated to distinct mechanism of lava lake formation

162   (see Introduction). The first phase (May 2014 to May 2016) was characterized by c_{rad}> 10^9 J/m^3

163   (Fig. 2d), a value much higher than the one typically measured during the flank lava-flow-forming

164   eruption of Nyamulagira 2-5 x 10^8 J/m^3 (Coppola and Cigolini, 2013; red field in Fig. 2d). We ascribe

165   this phase to the development of an active lava lake, whereby the excess of radiation is associated

166   to the convective circulation of magma at shallow depth. Conversely the second (December 2016

167   to May 2017) and third (April 2018 to April 2020) filling phases were characterized by a c_{rad} similar

168   to, if not even smaller than, the typical value characterizing the effusive regime. This is likely due

169   to the absence of magma convection and to the limited surface area of lava flows confined within

170   the pit, the thickness of which is controlled by geometric, rather than rheological, factors (Harris

171   and Baloga, 2009). Accordingly, we ascribe these two phases to the intermittent growth of an

172   inactive lava lake (blue field in Fig. 2d) whose detailed morphological evolution is described in the

173   next section and modelled in section 5.
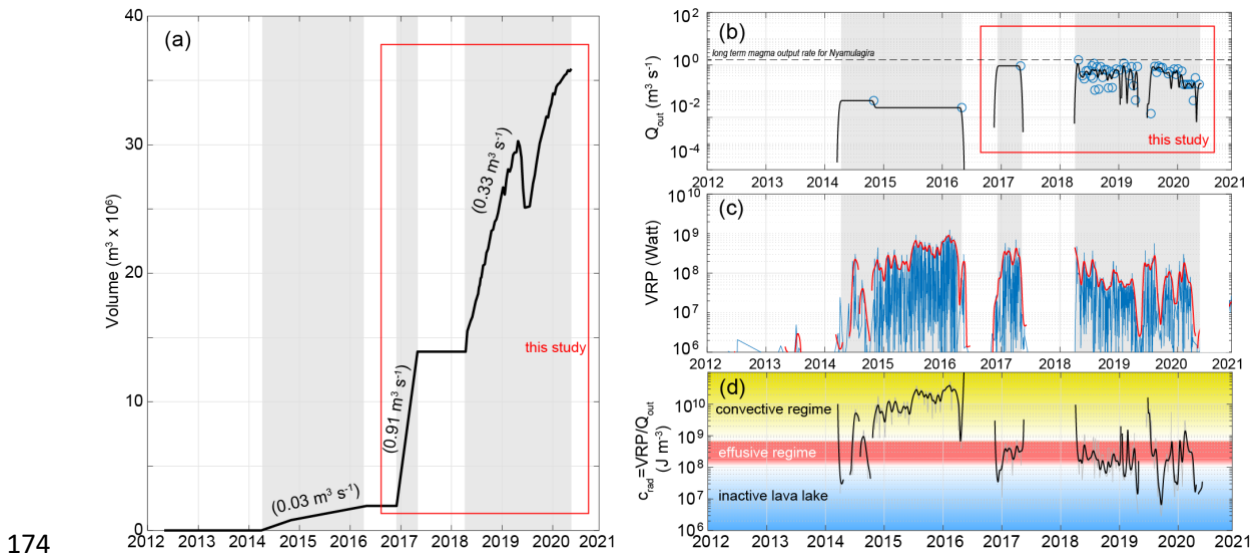
174

175   **Fig. 2.** (a) Cumulative volume of lava emplaced inside the summit crater of Nyamulagira between

176   the first appearance of a lava lake, in 2014 (Coppola et al., 2016a) and mid-2020. Three main

177   growth phases (grey fields) are defined by the respective time-averaged lava discharge rate (in

178   parenthesis). (b) The lava output rate (Q_{out}) associated to each phase is compared to the long-

179   term magma output rate (1.5 m^3/s) that characterized Nyamulagira effusive activity between 1980-

180   2012 (Aoki et al., 1985; Coppola et al., 2016a). (c) Volcanic Radiative Power (VRP) associated to

181   the three phases, as measured by the MIROVA system. (d) ratio between the radiant and

182   volumetric flux (c_{rad}=VRP/Q_{out}) throughout the analyzed period. Yellow and blue colored fields

183   refer to active and inactive lava lake mechanisms, respectively.

184   **4.2 Pit-crater activity between 2018-2020**

185   The third phase of growth (2018-2020), on which we focus in this study, was characterized by a

186   complex dynamic which we subdivided into three stages.

187   *4.2.1 Filling of the pit-crater (May 2018 – April 2019: Rise 1 phase)*

188   In May 2018 MIROVA thermal anomalies were suddenly detected after a nearly 1-year hiatus, and

189   the level of the pit-crater floor began to rise at a steady rate, as evidenced by the Sentinel-1 SAR

190   analysis (Fig. 3a,d) and field measurements.

191   Ground observations in July and November 2018 put in evidence intra-crateric lava flows taking

192   their origin either from a small lava lake (when present) or from hornitos (Fig. 4a,b & Supp. Fig.

193   S2). In February 2019, the small lava lake was located at the top of a convex surface that occupied

194   the whole crater and dominated the bottom of the cliffs from a height of about 15 m (Figs. 1b & 4b).

195   At this time, lava flows could be observed at the base of the pit-crater cliffs and occurred nearly

196   continuously during our 5-day stay (Fig. 4b).
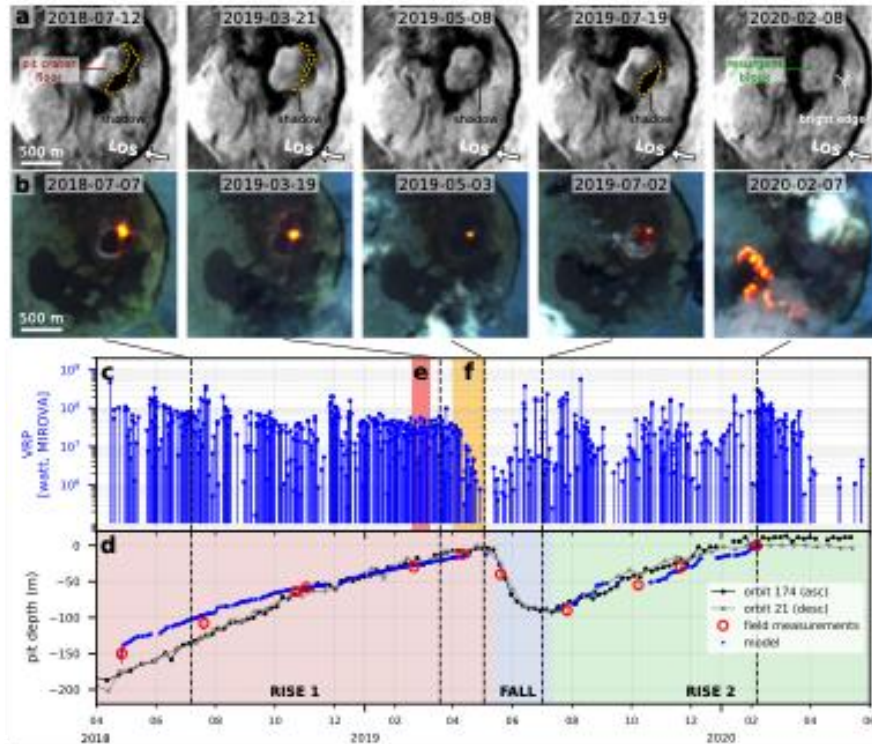
197

198   **Fig. 3.** Multiparametric data analysis. (a) Sentinel-1 SAR acquired in descending orbit (orbit 21,
199   line-of-sight LOS represented by white arrow), geocoded and speckle-filtered. The variations of the
200   shadow casted inside the pit crater (dashed yellow lines) highlight the variations of the crater depth.
201   (b) Sentinel-2 SWIR bands 12-11-8A. (c) Volcanic Radiative Power (VRP) measured from MODIS
202   TIR images (processed by MIROVA). (d) Pit crater depth estimated from field measurements (red
203   markers), Sentinel-1 SAR images with ascending and descending orbits in black and gray
204   respectively (processed by MOUNTS), and lava layers thickness modeling (blue line). The 3 phases
205   corresponding to the filling (Rise 1), emptying (Fall), and re-filling (Rise 2) of the pit-crater are
206   highlighted in red, blue and green respectively (as in Figure 4). (e) Timespan indicating when
207   deformation was measured by InSAR following a dyke intrusion under the caldera (Supp. Fig. S3).
208   (f) Timespan indicating a period when the thermal radiation decreased significantly, evidenced by
209   a drop in the VRP values and a decrease of the active lava lake dimensions.

210

211   From January 2019 to June 2019, tectonic seismicity around the Nyamulagira area shallower than

212   20 km was recorded by the seismic network of the Goma Volcanology Observatory (GVO). Many

213   inhabitants have reported experiencing earthquakes in the North (mostly from the City of Rutchuru,

214   located 35 km from Nyamulagira), and South of Nyamulagira, particularly in the lake Kivu area,

215   including the Goma City, with magnitudes up to 4.5. In February 2019, deformation inside the crater

216   was detected in three distinct interferograms, spanning from February 13 to March 9, 2019 (Fig.

217   3e). The InSAR deformation pattern suggests that a dyke firstly propagated from the pit crater

218   towards the South-East and accumulated under the most eastern-side of the caldera floor (Supp.

219   Fig. S3). No lava emissions were associated with this deformation episode, which resulted in a

220   maximum deformation in the radar line-of-sight of 8.4 cm. Shortly afterwards, the thermal activity

221   within the crater dropped significantly from April 12, 2019 to early May 2019 (Fig. 3f), as testified

222   by the decrease in VRP detections. Notably, the decrease in the lava lake size (which was 50 m

223   long and 30 m wide at the end of February 2019), and the disappearance of lava flows surrounding

224   the crater floor, visible already in July 2018 (Fig. 3b) were not accompanied by the subsidence of

225   the pit-crater floor but rather, by a slow upward rise (Fig. 3d).

226   *4.2.2 Subsidence of the pit-crater (May 2019 – June 2019: Fall phase)*

227   A radical change in the crater activity occurred in May 2019 with a large subsidence of the pit-crater

228   floor lasting 2 months (Fig. 3d, "Fall" phase). The first ground-based observation of this

229   phenomenon dates back to May 2019 with a floor subsiding by about 10 m with respect to its level

230   two months before. While no direct observations were reported, both MONUSCO, which makes

231   regular reconnaissance flights in this area, and local inhabitants reported rumbling and smoke from

232   inside the crater, that could correspond to the floor's detachment. MONUSCO also reported that a

233   camp inhabited for more than 10 years by a rebel group on the southern upper flank of the volcano

234   was suddenly abandoned in the second half of May 2019. However, as the closest seismic station

235   is 25 km away, the event did not yield discernible seismic signals, with the exception of two long-

236   period (LP) seismic swarms in May 8-9, 2019 and in May 16-19, 2019, which could be linked to the

237   first phases of the sinking of the pit-crater floor.

238   This subsidence reached -90 m at the end of July 2019 (Fig. 4c), representing a loss of a volume

239   of lava of about 8 x 10^6 m^3. No fractures of the pit-crater floor nor at its surroundings or outside the

240   crater on its flanks were observed, as it usually occurs during caldera collapses at basaltic shield

241   volcanoes (Derrien et al., 2020; Neal et al., 2019). The morphology of the pit crater floor with the

242   hornito in its center stayed surprisingly intact and kept degassing (Figure 4c). Two platforms located

243   in the northern part of the pit crater (P1 and P2, Fig. 1c), which had been covered with a lava layer

244   estimated to be 35 m thick during the filling of the pit crater in 2018, were cleared and became

245   partly visible again (Fig. 4c).

246   *4.2.3 Re-filling of the pit-crater and uplift of a solidified block (July 2019 – February 2020: Rise 2*

247   *phase)*

248   Following the subsidence phase, the pit-crater floor resumed rising at the end of July 2019 (Rise 2

249   phase), with the emplacement of lava flows at the bottom of the pit (Fig. 4c). Shortly after, the

250   bottom of the pit-crater appeared as a sub-circular 290 m x 390 m solidified block as attested by

251   the development of a large fracture (Fig. 4d & Supp. Fig. S4). This solidified block stayed intact

252   throughout this re-filling phase (fracture still visible in the 2020-03-03 satellite image, Fig. 4e &

253   Supp. Fig. S5a), suggesting that the block was being pushed from below similar to a piston-

254   mechanism, with an uplift rate in the order of cm per hour. In February 2020, the pit crater was

255   completely filled and lava was overflowing from its periphery onto the main caldera floor (Fig. 4e &

256   Supp. Fig. S5). At this time, the emergent solidified block protruded about 10 m above the caldera

257   floor (Fig. 4e). This protruded topography was also observable on Sentinel-1 SAR images, as the

258   pit-crater edge no longer appeared as a dark shadow (i.e. negative topography), but rather as a

259 thin bright edge, indicating the reflection of the radar electromagnetic wave onto a positive

260 topography (Fig. 3a).
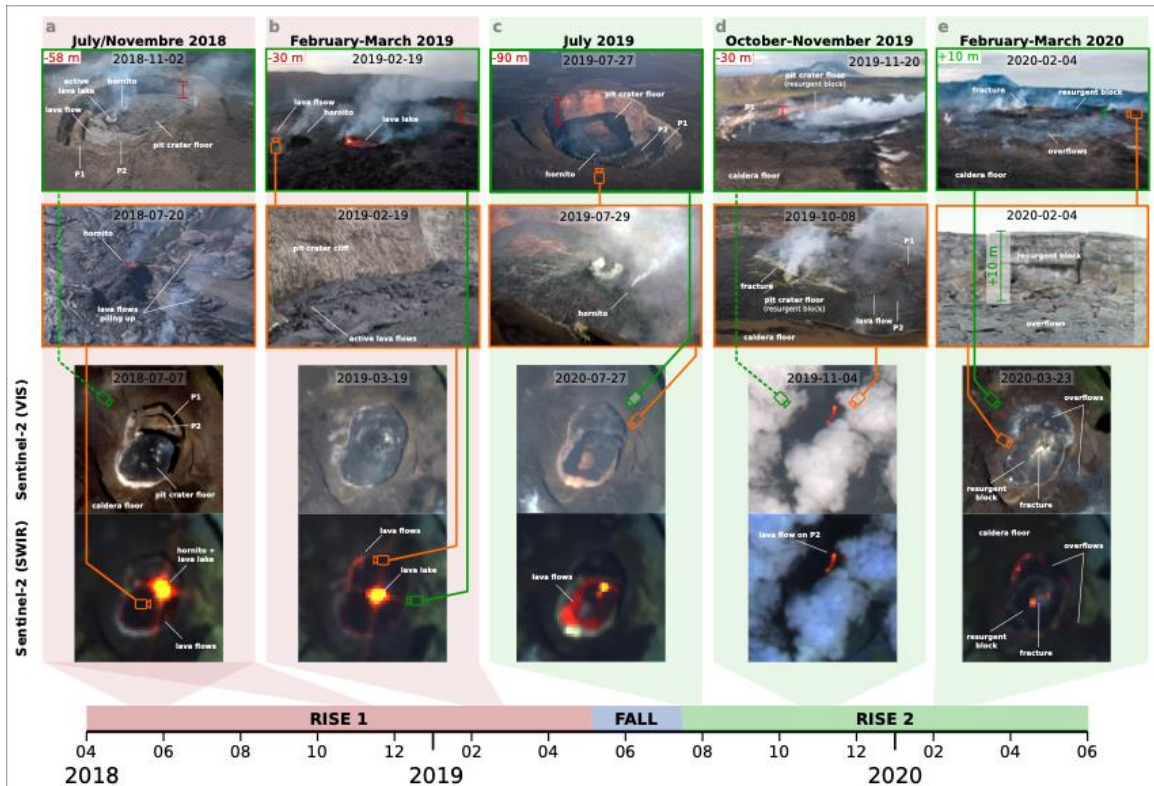
Fig. 4. Evolution of the pit crater morphology from April 2018 to June 2020 based on photographs and satellite images (Sentinel-2, optical and SWIR band combinations). The 3 phases corresponding to the pit-crater filling (Rise 1), emptying (Fall), and re-filling (Rise 2) are respectively represented in red, blue, and green (as in Fig. 3). Pictures from the authors.

5 Numerical Models

268 Based on the above-described multiparametric data, modeling was used to explain (i) the filling of

269 the pit crater, (ii) the subsidence that followed without evidence of brittle fracturing, (iii) the

270 emergence of a solidified block, and (iv) the state of crystallization of the successive layers based

271 on a thermal model. Note that only the period preceding subsidence (April 2016 to April 2019, Supp.

272   Fig. S1) is considered for the thermal model, as "rise 2" phase involves a piston effect not fully

273   accountable by a thermal model.

274   **5.1 Lava layer thickness**

275   We model the filling of the Nyamulagira crater from April 2016 to February 2020 not as a rising lava

276   lake, but rather as the stacking of a succession of distinct lava flows detected remotely by the

277   MIROVA system. We apply the following relation between the radiative energy *VRE* and the

278   erupted volume *V* (Coppola et al., 2013),

279   $c_{rad} = \frac{VRE\,\gamma}{V}$ (1)

280   where γ is a correction factor (set to 1.3) for compensating the thermal energy attenuation due to

281   the presence of clouds (frequent in this region), and c_{rad} is the radiant density, which characterizes

282   several properties of the lava emplacement, such as insulation, rheological and topographic

283   conditions. The particular geological context of these flow units (lava flows confined in a deep

284   crater) implies that, for a fixed effusion rate, these intra-crater lava flows will have a smaller surface

285   area than equivalent lava flows that are emplaced along the flank of the volcano (free to expand).

286   For the case of caldera confined lava emplacement, the thickness of the lava layers at day *n* may

287   be approximated by $H_n = V_n/(\pi r^2)$, with *r* the average pit crater radius. From equation (1), which

288   takes into account all radiative sources, including the presence of a small lava lake, we can express

289   the layer's thickness H_n as

290   $H_n = \frac{VRE_n\,H_{tot}}{VRE}$ (2)

291   with H_{tot} being the total lava flow thickness, and VRE_n corresponding to the radiative energy

292   calculated for each specific day *n*. To avoid unrealistic lava flows, a thickness smaller than 10 cm

293   is discarded. Consequently, the time separating two lava flows is determined by the occurrence of

294   layers thicker than this threshold value.

295   **5.2 Collapsing conditions**

296   According to visual observations performed in July 2019 (Fig. 4c), the floor's detachment has

297   occurred along a pit-crater segment with sub-vertical cliffs. We thus model it as a vertical piston

298   whose load is balanced by friction at the wall surrounding it. Also, the condition for a solid portion

299   of height H_s in contact with pit-crater walls to collapse is satisfied when the vertical load (F_v) (Duputel

300   and Rivera, 2019; Kumagai, 2001)

301     $F_v = \frac{\pi D^2 H_s \rho g}{4}$ (3)

302   with D the average pit-crater diameter, ρ the density of degassed magma, and g the gravity

303   acceleration, exceeds a critical shear force (F_s) given by (Roche and Druitt, 2001)

304     $F_s = \tau_c \pi H_s D,$ (4)

305   where τ_c is the critical shear stress for rupture, taken to follow the Coulomb fracture criterion

306   (Nicholson, 1994),

307     $\tau_c = \tau_0 + \mu \frac{\nu}{1-\nu} \frac{\rho g H_s}{2},$ (5)

308   with ν the Poisson's ratio and μ the sliding friction. Because the pit crater was filled by successive

309   lava layers, and that lava may be oozing at the edges and thus lubricating some contact points,

310   cohesion τ_0 is estimated to be 1-2 orders of magnitude lower than the value for intact basalt

311   (Schultz, 1995). To be conservative, we set $\tau_0 = 1 \times 10^6$ Pa. Combining the last three equations,

312   the collapse condition $F_v > F_s$ is verified for

313 $\quad H_s < \frac{1-\nu}{\mu\upsilon}\left(\frac{D}{2} - \frac{2\tau_0}{\rho g}\right)$ (6)

314 With the parameters reported in Table 1, we estimate a total solid layer height $H_s < 423$ m. Later

315 in Section 4.2 we show that the solid layers are all much smaller than this value, which indicates

316 that the collapsing condition is always satisfied once the underlying pressure drops.

317 **5.3 Heat equation**

318 Based on ground observations (Fig. 4 & Supp. Fig. S2), we take for granted that magma erupts by

319 successive lava flows, the initial one with thickness H_1 at liquidus temperature T_{liq}. By heat radiation

320 and convection within the surrounding atmosphere T_{atm}, cooling of the lava surface starts and

321 proceeds by conduction toward the lava interior, with latent heat released inside the lava layers

322 due to crystallization. A new lava flow covers the previous layer with thickness H_2, and the process

323 repeats until the crater is filled. The layer thickness H_n (equation 2) and the lava flows' occurrence

324 time t_n are both evaluated based on the radiant density estimated from MIROVA data.

325 Temperature and melt fraction of the lava layers are computed using the finite difference expression

326 of the heat equation. Given the horizontal spatial extent of the pit crater (several hundreds of

327 meters) and duration of the considered period, we assume that the horizontal heat loss at the crater

328 walls does not affect the vertical temperature distribution, and thus a one-dimensional model can

329 be applied. This assumption is at least reasonable for the central part of the crater under study. To

330 calculate the temporal and spatial evolution of temperature $T(X, t)$ of this central part that

331 experiences repeated accumulation of lava flows, we apply the heat equation, derived by combining

332 the conservation of energy and Fourier's law

333 $\quad k\frac{\partial^2 T}{\partial X^2} = \rho c_p \frac{\partial T}{\partial t} - \rho L \frac{\partial f_c}{\partial t}$ (7)

334   where (see Table 1) f_c is melt fraction (which depends on temperature), k is thermal conductivity,

335   ρ is the density, c_p is specific heat capacity, *L* is latent heat, *t* is time, and X is vertical distance,

336   which increases after each lava flow.

337   To best match available data on the rheology of Nyamulagira's lavas (Morrison et al., 2020),

338   variation of the crystallinity with temperature *T* is approximated by a nonlinear function,

339    $f_c = a + b \sinh(c \frac{T - T_{sol}}{T_{liq} - T_{sol}} + d)$ (8)

340   with T_{sol} the solidus temperature, which for many magmas is observed to correspond to $T_{liq} - 200$

341   (Marsh, 1981; Wright and Marsh, 2016), and T_{liq} is set to 1260 ºC (Morrison et al., 2020). This

342   function yields slow crystallization within the first 80-100 ºC subliquidus, and then changes regime

343   with a fast increase in the rate of crystallization. While the absolute temperature of this interval

344   shifts to lower temperatures with decreasing oxygen fugacity, the width of this temperature interval

345   remains similar (Kolzenburg et al., 2020, 2018a). Substituting this definition for f_c in equation (7),

346   we get

347    $\frac{\partial^2 T}{\partial X^2} = \frac{\partial^2 T}{\partial X^2} = \frac{\rho}{k}\left[c_p - \frac{L\,b\,c}{T_{liq} - T_{sol}}\cosh(c\frac{T - T_{sol}}{T_{liq} - T_{sol}} + d)\right]\frac{\partial T}{\partial t}$ (9)

348   with parameters *a*, *b*, *c* and *d* in Table 1. With the chosen parameters, the "cut-off" temperature

349   where crystallization exponentially increases (Kolzenburg et al., 2016) is at 1180 ºC. The heat flux

350   from the lava surface ($X = 0$) is described by a boundary condition, which we take

351    $\sigma\varepsilon(T^4 - T_{atm}^4) - k\frac{\partial T}{\partial x} = 0$ (10)

352   where the first term stands for the radiant heat flux, with σ the Stefan-Boltzmann constant and ε

353   the emissivity of the lava surface, and the second term stands for heat transfer by conduction. It

354   must be noted that we neglected heat transfer by natural convection in this equation as heat lost

355   by radiant heat flux is several orders of magnitude larger for the range of considered temperatures.

356   On the other hand, latent heat, liberated as lava solidifies, has a significant effect and provides a

357   large quantity of energy per unit mass that delays cooling.

358   To keep computation time reasonable, equations (9) and (10) were discretized on a spatial mesh

359   of 2.5 cm (the thinnest lava flow being 10 cm) and time increment fixed to 8 minutes. These settings

360   verify the mesh Fourier number criterion (Smith et al., 1985): for the considered heat equation this

361   criterion is given by $F = \frac{k}{\rho c_p} \Delta t / \Delta x^2$, which yields 0.49, verifying the stability condition F < 0.5. At

362   the occurrence of each lava flow, whose time of occurrence and thickness (see above) were derived

363   from the MIROVA data, the equation is reinitialized with new initial and boundary conditions, which

364   corresponds to instantaneously emplaced lava.

365   **Table 1 HERE**. Physical properties and parameters employed in the model.

366   **6 A stratified pit crater highlighted by numerical modeling**

367   The numerical solutions of the thermal model (vertical thermal profile) during the April 2016 - April

368   2019 period, reveal that just before the subsidence occurred in May-June 2019, the pit crater

369   consisted of an alternation of molten and solidified layers (Fig. 5b). Of the 290 m of lava piled up

370   during this period, about 160 m were solidified (cf. S1 to S5 on Fig. 5b) and 130 m were in a molten

371   state (cf. M1-M4 on Fig. 5b). The preservation of molten layers results mainly from the effect of the

372   latent heat generated during the cooling and solidification of other layers. Without this effect, almost

373   the entire pit crater would be solidified (Supp. Fig. S6). We argue that molten layers interspersed

374   between solid layers promote the collapse of the crater and accelerate the phenomenon (by

375   draining the molten layers – Fig. 5c). On contrary, the displacement of a 300 m rock thickness will

376   generate much more friction against the wall. While being conservative in the values of equation 6,

377 a thickness of 300 m is closer to the limit value (423 m), which might potentially be overvalued.

378 Moving thinner solid layers more easily meets the dropout condition.

379 The layer thickness evolution (described by equation 2 and inferred from MIROVA) closely fits the

380 field and satellite observations (Fig. 3b & Supp. Fig. S7) although the 2-3 m individual layers (middle

381 panel of Fig. 4e) and Supplementary Figure S4a cannot be resolved through the heat equation

382 solutions (e.g., Fig. 5b). This would have required the inclusion of layer boundary formation

383 mechanisms and intra-layer vertical variations (grain size, mineral compositions, textures, etc.

384 present in the layers) in the model that involve a wide variety of factors (Naslund and McBirney,

385 1996), which was not the focus of this study.

386 Because thermal parameters are rarely provided for specific volcanoes, and Nyamulagira is not an

387 exception, a sensitivity analysis was used to confirm the consistency of the results obtained (Table

388 1). No appreciable effect on the distribution of the solid layers in the stacked column have been

389 observed (Supp. Fig. S8), and the predominant variables turn out to be the timing and thickness of

390 the lava flow, both derived from MIROVA data. A similar observation has been reported for

391 incremental intrusions in sills in which the rate of basalt emplacement (represented here by the

392 timing and thickness of the lava flows) is an important variable in determining melt fraction (Annen,

393 2011; Jackson et al., 2018).
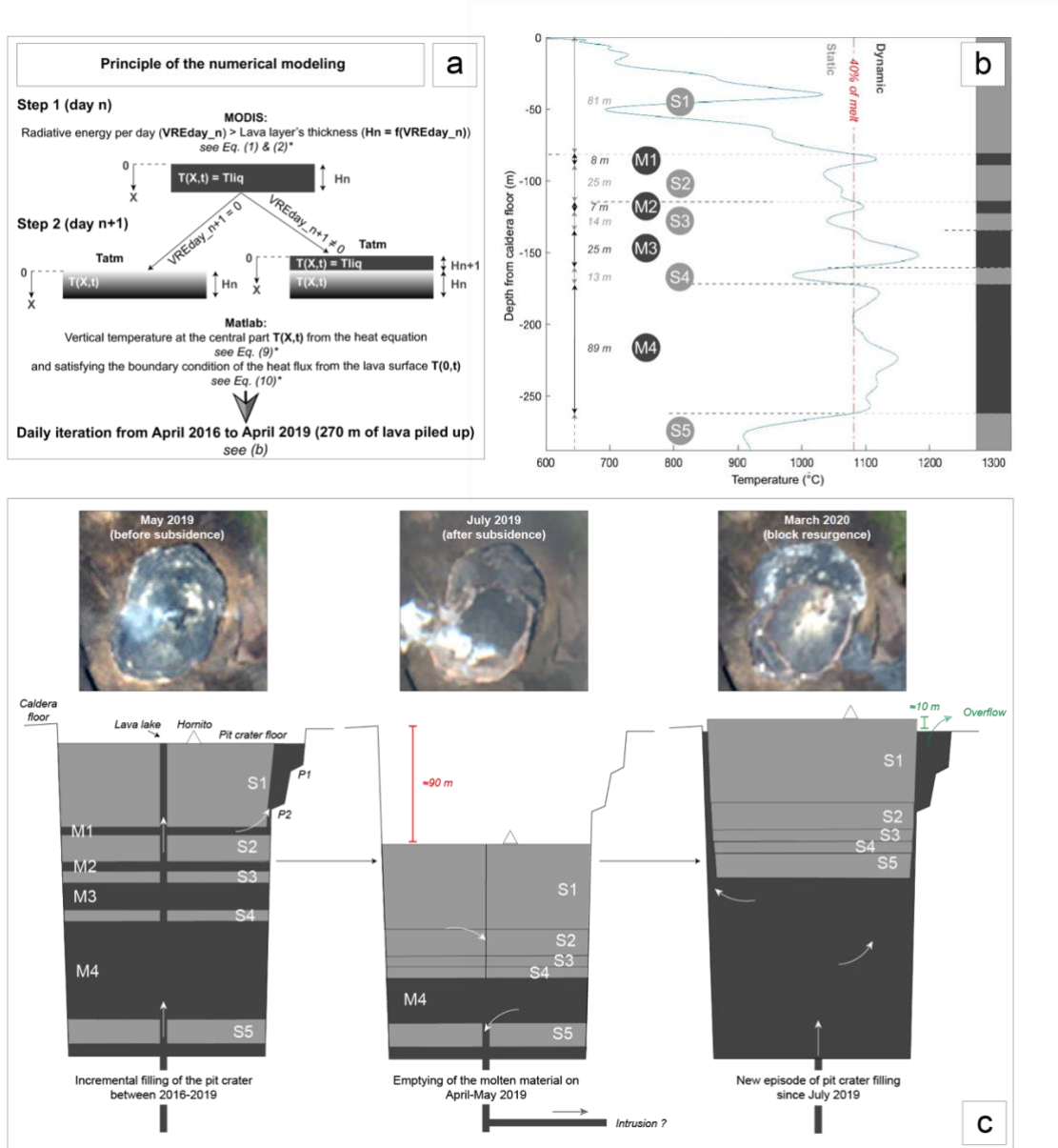
Fig. 5. Thermal modelling with the resulting collapse and emergence of the solid block scenario. (a) Description of the main principles used in numerical modeling. Equations (*) are described in Section 5. (b) Result of the numerical modeling (temperature profile) performed between April 2016 and April 2019 (about 1000 days) to simulate the state (S: solid vs. M: molten layers) of the pit crater filled by 290 m of lava before its subsidence. The dashed red line indicates 40% melt fraction (below this line the lava is supposed to be static and above it flowing). (c) Interpretative scheme (not at scale) of the evolution of the pit crater before and after the subsidence (May 2019 - March 2020) together with Sentinel-2 images.

403 **7 Discussion**

404 The morphology of the pit crater and filling mode since April 2016 have led to the layering of lava

405 with different states of solidification. The numerical solution of the thermal model (Fig. 5) shows

406 that before the subsidence of May 2019 (i) a large part of the pit crater (~130 m) was filled with

407 molten lava; (ii) the first 80 m upper segment of the pit crater is mostly solid, with a melt fraction

408 smaller than 40%, and is thus too viscous to flow (Annen, 2011; Kolzenburg et al., 2018b; Lamy-

409 Chappuis et al., 2020; Lejeune and Richet, 1995; Marsh, 1981; Sparks et al., 2019); (iii) under this

410 solid crust reside several molten lava layers, the largest one being over 90 m thick, interspaced by

411 solidified layers up to 25 m thick (Fig. 5b). We now discuss how this layer structure impacts the

412 subsidence of the pit-crater (May – June 2019) and the following uplift of a solidified block (July

413 2019 - February 2020).

414 **7.1 Subsidence and emergence mechanisms**

415 Subsidence of the crater floor, which started in May 2019 and lasted 2 months (Fig. 3d), is most

416 probably associated with lava draining from the shallow magmatic system. Although the origin of

417 such draining is still unclear and outside the scope of this study, it is worth noting that this

418 subsidence was preceded, 6 weeks before (in March 2019), by a small intrusion evidenced by

419 InSAR (originating from the pit-crater and extending under the caldera floor, Supp. Fig. S3),

420 concomitant to recorded tectonic earthquakes. Nevertheless, the intrusive episode was followed by

421 a month-long reduction of the thermal flux (Figs. 2c & 3c) possibly indicating a break in the

422 magmatic supply or a partial drainage of the magma column caused by the intrusion below the

423 caldera floor. It should be noted that this decrease of magma supply to the surface did not cause

424 the immediate collapse of the crater which began to subside only one month later, in early May

425 2019 (Fig. 3d). The following subsidence lowered the pit-crater floor of about 90 m (Figs. 3d & 4c),

426 a value that can be explained by our model as it corresponds to the drainage of almost all the
427 melted layers interspersed in the pit crater (Fig. 5c).

428 Ground observations suggest that the central part of the pit crater has sunk as a single solid block
429 (as a piston), a feature that makes this subsidence episode similar to a caldera collapse. Moreover,
430 the time delay between the observed deformation and subsidence is reminiscent of caldera
431 collapses where faulting can precede subsidence by several days to weeks (Derrien et al., 2020;
432 Shelly and Thelen, 2019).

433 Caldera collapses, with subsequent resurgence of domes, share similar characteristics with those
434 modeled here (Smith and Bailey, 1968): (i) Nyamulagira follows a piston model with a solid block
435 of plane-like and of sub-circular shape, where subsidence begins when gravity exceeds the
436 frictional forces with the surrounding wall rock (Duputel and Rivera, 2019; Kumagai, 2001; Michon
437 et al., 2011); (ii) fracturing of the subsiding blocks has been observed to depend on the ratio block's
438 thickness (T) to diameter (D) - in our case we estimate T/D=0.35, which tends to favor sagging as
439 a single central block subsidence (piston) style with well-defined ring faults, which would not be the
440 case for much thinner crust (for which T/D<0.3) (Holohan et al., 2013, 2011; Roche et al., 2000).
441 With such a thickness (160 m, Fig. 5c), the underlying magmatic column remains confined beneath
442 the crust, except for intrusions around the block, which was actually observed (panel July 27, 2019
443 in Figure S5B); (iii) uplift of a solid block is favored by a crystallized front, which serves as a
444 rheological barrier whereby magma intrusions accumulate and exerts an upward pressure (Galetto
445 et al., 2017); (iv) any subsequent increase in magma volume potentially causes surface volcanism
446 concomitantly with the uplift of the emergent block (or injection of magma into fracture systems);
447 (v) low-viscosity magma would tend to dissipate magma pressure adjacent to the emergent block
448 with consequent surface volcanism.

449   Besides the involved spatial scale much smaller than in caldera forming volcanic settings, two main

450   differences can be highlighted: (1) subsidence is linked to the drainage of molten layers (Fig. 5c) in

451   addition to the piston effect, which could accelerate subsidence; (2) uplift of the solid block occurred

452   at a faster and constant rate of cm/hour instead of cm/year (Dvorak and Dzurisin, 1997; Geist et

453   al., 2006; Métrich et al., 2011; Ukawa et al., 2006).

454   The uplift of the solid block formed by the compaction of the remaining solidified layers (Fig. 5c),

455   which are lighter and cooler than the hottest and least differentiated magma (Sparks and Huppert,

456   1984), could be favored by an increase of the magma flow, and thus upward pressure. Taking the

457   hydrostatic pressure $\rho g H$, where ρ and H are, respectively, the density and thickness of the solid

458   block (Fig. 5c), and taking into account the friction force against the cliffs (equation 4), then about

459   7 MPa are required to make it resurface (the hydrostatic pressure counting for 60%). This

460   represents an upper bound as most likely molten lava was interposed between the cliffs and the

461   block (which explains the lava flows on the edge of the crater floor, e.g. Fig. 4), thereby reducing

462   the frictional forces. The uplift of the solid block started in mid-July 2019 and was again

463   accompanied by LP earthquake swarms at depth similar to those recorded in May 2019.

464   Concomitant to the block uplift, fresh lavas flooded the area around it and finally overflowed the

465   caldera floor in February 2020 (Fig. 4e and injection along the margins of the solidified surfaces on

466   Supp. Fig. S5b).

467   According to Fig. 5c, there are no more interspaced molten layers and the whole piston is in contact

468   with the magma column.

469   **7.2 Towards an unconventional model of pit crater filling**

470   The thermal model reveals a filling mechanism of the pit crater by successive solid and liquid layers

471   whose thickness depends on frequency and size of the lava flows and size of the pit crater. This

472 filling pattern characterize the inactive lava lakes and is unconventional in the sense that it can be

473 defined as alternative to both (1) a purely convective mode, where the convection disrupts solid

474 layers (active lava lake, yellow zone on Fig. 2d) and (2) an effusive mode, where single flow units

475 have time to solidify before stacking up (blue zone on Fig. 2d). This unconventional mode, which

476 we call "streaky", is represented schematically in Fig. 6. Our model further highlights a filling

477 mechanism that could occur in other craters. For example the neighboring Nyiragongo volcano,

478 whose crater has been filled both by overflows of the lava lake (which also occupies only a portion

479 of its floor surface) and by intra-crateric eruptions that began in 2016 with the formation of a new

480 spatter cone (Burgi et al., 2020, 2018), shows great similitudes with Nyamulagira. However, no

481 similar subsidence or block uplift has been observed, probably due to the different physical

482 configuration of the crater and the underlying convective magma column.

483 Thermal models of discrete emplacement units of magma have previously been proposed to

484 explain the formation of magma reservoirs and plutons (Annen, 2011; Annen and Sparks, 2002;

485 Biggs and Annen, 2019; Blundy and Annen, 2016; Jackson et al., 2018; Michaut and Jaupart, 2011;

486 Sparks et al., 2019). A common feature of these models is the magma emplacement modality,

487 assumed to occur piecemeal with small increments rather than in a single large event. However,

488 these thermal models are based on the following assumptions that are not applicable in our case:

489 (i) successive magma injection through sills occurring upwards and downwards (Annen, 2011); (ii)

490 the layers being intruded are not subject to radiative heat loss and cooling is mainly done by

491 conductive loss; (iii) thick magma bodies may develop convective instabilities which accelerate

492 cooling (Simakin and Trubitsyn, 1995); (iv) timescales are tens to hundreds of thousands of years,

493 and spatial dimensions range on kilometer scale.

494 Solidification of lava lakes (Colp, 1982; Helz et al., 2014; Worster et al., 1993; Wright et al., 1976;

495 Wright and Marsh, 2016), which starts once the magma influx needed to keep the molten state

496   strongly decreases or ceases, represents another situation governed by thermal equations similar

497   to those applied in our model. However, in the case of lava lake, the solidified surface crust

498   preventing further radiative heat loss and cooling is mainly controlled by heat transfer by conduction

499   to the host rocks, and through the upper crust of the lake to the air, corresponding to ε=0 in equation

500   (10). For stagnant lava ponds, such as the Kilauea inactive lava lakes (Wright et al., 1976), lava is

501   accumulated through successive eruptive phases. Also, crust solidification is much slower in lava

502   ponds than in our case: more than 7 years to solidify 80 m against less than 6 months in our case

503   (Helz et al., 2014; Wright et al., 1976). A common feature though is the density profile with depth,

504   where the cooled crust is lighter than the underlying hot melt.
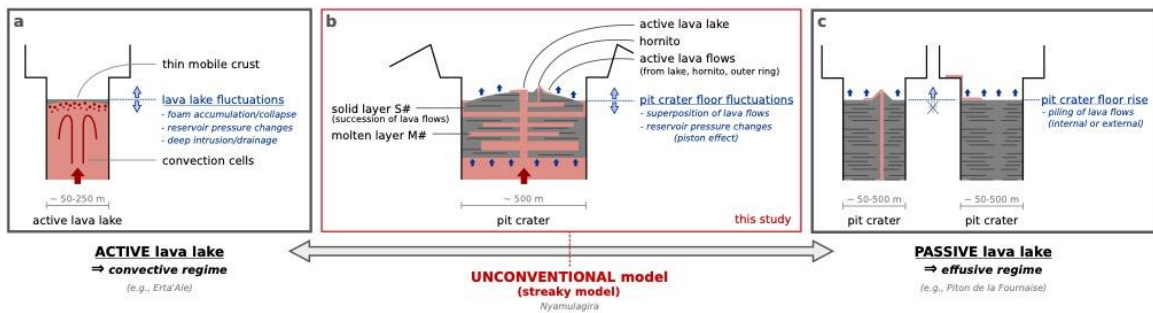
505

506   **Fig. 6.** Conceptual models used to explain depth variations of pit-craters. (a) Active lava lake model,

507   whereby the pit-crater hosts an active lava lake with convective cells: depth variations are

508   commonly explained by foam accumulation/collapse beneath a thin solid crust, and/or pressure

509   changes in the magma column/reservoir ("piston-effect"), and/or deep intrusion and magma column

510   drainage (Patrick et al., 2019). (b) Unconventional "streaky" model presented in this study, whereby

511   the pit-crater is filled by interleaved solid and molten layers: the depth fluctuations are explained by

512   both the piling of lava flows, and by variations of the magma column/reservoir pressure. (c) Passive

513   lava lake, whereby the pit-crater is filled passively by piling of lava flows from vents located inside

514 and/or outside the pit: the pit-crater floor does not fluctuate up/down, but only rises depending on

515 the effusive activity alone.

516 **4 Conclusions**

517 This case study, based on field and satellite measurements, and numerical modelling, shows a new

518 crater filling dynamic: while being in close contact with a magma column, Nyamulagira's pit crater

519 fills up incrementally by the overlapping of intra-crateric lava flows. This mechanism results in the

520 formation of solidified layers, interspersed with partially molten flow units, whose characteristics

521 depend on the temporal spacing between each emission of lava. Such an incremental filling of the

522 crater creates the conditions for the unconventional collapse and buoyant ascent of the solidified

523 layers, both of which constitute novel processes within pit craters. Our model thus contributes to

524 extend and improve our knowledge on processes underlying the dynamics of pit craters containing

525 lava lakes.

526 While the volcanic phenomena reported here are confined to the caldera, the underlying pressure

527 variations of the magmatic reservoir should be acknowledged as serious hazard for the region's

528 continuous population growth in the most western side of the Virunga Volcanic Province. Indeed,

529 lava flows generated by Nyamulagira directly threaten the city of Sake with a population of over

530 100,000 inhabitants (located 25 km from the volcano), and potentially lead to severe logistical

531 supply problems by cutting the only road that links Goma (the capital of North Kivu, population >1

532 million, located at about 30 km south east of the volcano) to the western and southern territories of

533 north and south Kivu (Balagizi et al., 2018; Patrick et al., 2019; Tedesco et al., 2007), as shown by

534 the recent event of the nearby Nyiragongo in May 2021.

535 **Acknowledgments**

550

551   **Code and Data Availability**

552   All data generated or analyzed during this study are provided with this article, and are available at

553   https://doi.org/10.26037/yareta:khivh7h2prgvxauarlckdo7awi

554   MIROVA data, and the associated codes for computing the thickness and time of occurrence of the

555   lava flows, as well as thermal evolution of the lava layers are available at

556   https://doi.org/10.26037/yareta:5futgivyezdw5gdqqfogybt3ky

557   Sentinel-1 and Sentinel-2 data used in this study are available and freely downloadable from the

558   Copernicus Open Access Hub (https://scihub.copernicus.eu/).

References

Annen, C., 2011. Implications of incremental emplacement of magma bodies for magma differentiation, thermal aureole dimensions and plutonism–volcanism relationships. Tectonophysics 500, 3–10. https://doi.org/10.1016/j.tecto.2009.04.010

Annen, C., Sparks, R.S.J., 2002. Effects of repetitive emplacement of basaltic intrusions on thermal evolution and melt generation in the crust. Earth Planet. Sci. Lett. 203, 937–955. https://doi.org/10.1016/S0012-821X(02)00929-9

Aoki, K.-I., Yoshida, T., Yusa, K., Nakamura, Y., 1985. Petrology and geochemistry of the Nyamuragira volcano, Zaire. J. Volcanol. Geotherm. Res. 25, 1–28. https://doi.org/10.1016/0377-0273(85)90002-2

Balagizi, C.M., Kies, A., Kasereka, M.M., Tedesco, D., Yalire, M.M., McCausland, W.A., 2018. Natural hazards in Goma and the surrounding villages, East African Rift System. Nat. Hazards 93, 31–66. https://doi.org/10.1007/s11069-018-3288-x

Barrière, J., d'Oreye, N., Oth, A., Geirsson, H., Mashagiro, N., Johnson, J.B., Smets, B., Samsonov, S., Kervyn, F., 2018. Single-Station Seismo-Acoustic Monitoring of Nyiragongo's Lava Lake Activity (D.R. Congo). Front. Earth Sci. 6, 82. https://doi.org/10.3389/feart.2018.00082

Biggs, J., Annen, C., 2019. The lateral growth and coalesence of magma systems. Philos. Trans. R. Soc. Math. Phys. Eng. Sci. 377, 20180005. https://doi.org/10.1098/rsta.2018.0005

Blundy, J.D., Annen, C.J., 2016. Crustal Magmatic Systems from the Perspective of Heat Transfer. Elements 12, 115–120. https://doi.org/10.2113/gselements.12.2.115

Bluth, G.J.S., Carn, S.A., 2008. Exceptional sulfur degassing from Nyamuragira volcano, 1979–2005. Int. J. Remote Sens. 29, 6667–6685. https://doi.org/10.1080/01431160802168434

Burgi, P. -Y., Boudoire, G., Rufino, F., Karume, K., Tedesco, D., 2020. Recent Activity of Nyiragongo (Democratic Republic of Congo): New Insights From Field Observations and Numerical Modeling. Geophys. Res. Lett. 47. https://doi.org/10.1029/2020GL088484

Burgi, P.-Y., Caillet, M., Haefeli, S., 2002. Field temperature measurements at Erta'Ale Lava Lake, Ethiopia. Bull. Volcanol. 64, 472–485. https://doi.org/10.1007/s00445-002-0224-3

Burgi, P.-Y., Minissale, S., Melluso, L., Mahinda, C.K., Cuoco, E., Tedesco, D., 2018. Models of the Formation of the 29 February 2016 New Spatter Cone Inside Mount Nyiragongo. J. Geophys. Res. Solid Earth 123, 9469–9485. https://doi.org/10.1029/2018JB015927

589 Campion, R., 2014. New lava lake at Nyamuragira volcano revealed by combined ASTER and OMI
590   SO$_2$ measurements. Geophys. Res. Lett. 41, 7485–7492.
591   https://doi.org/10.1002/2014GL061808

592 Colp, J.L., 1982. Magma Energy Research Project. Sandia Natl. Lab. Albuq. N. M., Sandia Report
593   SAND82-2377 42.

594 Coppola, D., Campion, R., Laiolo, M., Cuoco, E., Balagizi, C., Ripepe, M., Cigolini, C., Tedesco, D.,
595   2016a. Birth of a lava lake: Nyamulagira volcano 2011–2015. Bull. Volcanol. 78, 20.
596   https://doi.org/10.1007/s00445-016-1014-7

597 Coppola, D., Cigolini, C., 2013. Thermal regimes and effusive trends at Nyamuragira volcano (DRC)
598   from MODIS infrared data. Bull. Volcanol. 75, 744. https://doi.org/10.1007/s00445-013-
599   0744-z

600 Coppola, D., Laiolo, M., Cigolini, C., Donne, D.D., Ripepe, M., 2016b. Enhanced volcanic hot-spot
601   detection using MODIS IR data: results from the MIROVA system. Geol. Soc. Lond. Spec.
602   Publ. 426, 181–205. https://doi.org/10.1144/SP426.5

603 Coppola, D., Laiolo, M., Piscopo, D., Cigolini, C., 2013. Rheological control on the radiant density
604   of active lava flows and domes. J. Volcanol. Geotherm. Res. 249, 39–48.
605   https://doi.org/10.1016/j.jvolgeores.2012.09.005

606 Derrien, A., Peltier, A., Villeneuve, N., Staudacher, T., 2020. The 2007 caldera collapse at Piton de
607   la Fournaise: new insights from multi-temporal structure-from-motion. Volcanica 3, 55–
608   65. https://doi.org/10.30909/vol.03.01.5565

609 Duffell, H.J., Oppenheimer, C., Pyle, D.M., Galle, B., McGonigle, A.J.S., Burton, M.R., 2003. Changes
610   in gas composition prior to a minor explosive eruption at Masaya volcano, Nicaragua. J.
611   Volcanol. Geotherm. Res. 126, 327–339. https://doi.org/10.1016/S0377-0273(03)00156-
612   2

613 Duputel, Z., Rivera, L., 2019. The 2007 caldera collapse of Piton de la Fournaise volcano: Source
614   process from very-long-period seismic signals. Earth Planet. Sci. Lett. 527, 115786.
615   https://doi.org/10.1016/j.epsl.2019.115786

616 Dvorak, J.J., Dzurisin, D., 1997. Volcano geodesy: The search for magma reservoirs and the
617   formation of eruptive vents. Rev. Geophys. 35, 343–384.
618   https://doi.org/10.1029/97RG00070

619 Galetto, F., Acocella, V., Caricchi, L., 2017. Caldera resurgence driven by magma viscosity
620   contrasts. Nat. Commun. 8, 1750. https://doi.org/10.1038/s41467-017-01632-y

621 Geist, D., Chadwick, W., Johnson, D., 2006. Results from new GPS and gravity monitoring networks
622   at Fernandina and Sierra Negra Volcanoes, Galápagos, 2000–2002. J. Volcanol. Geotherm.
623   Res. 150, 79–97. https://doi.org/10.1016/j.jvolgeores.2005.07.003

624 Harris, A.J.L., 2009. The pit-craters and pit-crater-filling lavas of Masaya volcano. Bull. Volcanol.
625   71, 541–558. https://doi.org/10.1007/s00445-008-0241-y

626 Harris, A.J.L., 2008. Modeling lava lake heat loss, rheology, and convection: MODELING LAVA LAKE
627   HEAT LOSS, RHEOLOGY, AND CONVECTION. Geophys. Res. Lett. 35, n/a-n/a.
628   https://doi.org/10.1029/2008GL033190

629 Harris, A.J.L., Baloga, S.M., 2009. Lava discharge rates from satellite-measured heat flux. Geophys.
630   Res. Lett. 36, L19302. https://doi.org/10.1029/2009GL039717

631 Harris, A.J.L., Flynn, L.P., Rothery, D.A., Oppenheimer, C., Sherman, S.B., 1999. Mass flux
632   measurements at active lava lakes: Implications for magma recycling. J. Geophys. Res.
633   Solid Earth 104, 7117–7136. https://doi.org/10.1029/98JB02731

634 Helz, R.T., Clague, D.A., Sisson, T.W., Thornber, C.R., 2014. Petrologic insights into basaltic
635   volcanism at historically active Hawaiian volcanoes (USGS Numbered Series No. 1801–6),
636   Petrologic insights into basaltic volcanism at historically active Hawaiian volcanoes,
637   Professional Paper. U.S. Geological Survey, Reston, VA. https://doi.org/10.3133/pp18016

638 Holohan, E.P., Schöpfer, M.P.J., Walsh, J.J., 2011. Mechanical and geometric controls on the
639   structural evolution of pit crater and caldera subsidence. J. Geophys. Res. 116, B07202.
640   https://doi.org/10.1029/2010JB008032

641 Holohan, E.P., Walter, T.R., Schöpfer, M.P.J., Walsh, J.J., van Wyk de Vries, B., Troll, V.R., 2013.
642   Origins of oblique-slip faulting during caldera subsidence: OBLIQUE-SLIP FAULTING AT
643   CALDERAS. J. Geophys. Res. Solid Earth 118, 1778–1794.
644   https://doi.org/10.1002/jgrb.50057

645 Jackson, M.D., Blundy, J., Sparks, R.S.J., 2018. Chemical differentiation, cold storage and
646   remobilization of magma in the Earth's crust. Nature 564, 405–409.
647   https://doi.org/10.1038/s41586-018-0746-2

648 Kolzenburg, S., Di Genova, D., Giordano, D., Hess, K.U., Dingwell, D.B., 2018a. The effect of oxygen
649   fugacity on the rheological evolution of crystallizing basaltic melts. Earth Planet. Sci. Lett.
650   487, 21–32. https://doi.org/10.1016/j.epsl.2018.01.023

651 Kolzenburg, S., Giordano, D., Cimarelli, C., Dingwell, D.B., 2016. In situ thermal characterization of
652   cooling/crystallizing lavas during rheology measurements and implications for lava flow

653   emplacement. Geochim. Cosmochim. Acta 195, 244–258.
654   https://doi.org/10.1016/j.gca.2016.09.022

655   Kolzenburg, S., Giordano, D., Hess, K.U., Dingwell, D.B., 2018b. Shear Rate-Dependent
656   Disequilibrium Rheology and Dynamics of Basalt Solidification. Geophys. Res. Lett. 45,
657   6466–6475. https://doi.org/10.1029/2018GL077799

658   Kolzenburg, S., Hess, K.-U., Berlo, K., Dingwell, D.B., 2020. Disequilibrium Rheology and
659   Crystallization Kinetics of Basalts and Implications for the Phlegrean Volcanic District.
660   Front. Earth Sci. 8, 187. https://doi.org/10.3389/feart.2020.00187

661   Kumagai, H., 2001. Very-Long-Period Seismic Signals and Caldera Formation at Miyake Island,
662   Japan. Science 293, 687–690. https://doi.org/10.1126/science.1062136

663   Lamy-Chappuis, B., Heinrich, C.A., Driesner, T., Weis, P., 2020. Mechanisms and patterns of
664   magmatic fluid transport in cooling hydrous intrusions. Earth Planet. Sci. Lett. 535,
665   116111. https://doi.org/10.1016/j.epsl.2020.116111

666   Lejeune, A.-M., Richet, P., 1995. Rheology of crystal-bearing silicate melts: An experimental study
667   at high viscosities. J. Geophys. Res. Solid Earth 100, 4215–4229.
668   https://doi.org/10.1029/94JB02985

669   Lev, E., Ruprecht, P., Oppenheimer, C., Peters, N., Patrick, M., Hernández, P.A., Spampinato, L.,
670   Marlow, J., 2019. A global synthesis of lava lake dynamics. J. Volcanol. Geotherm. Res.
671   381, 16–31. https://doi.org/10.1016/j.jvolgeores.2019.04.010

672   Marsh, B.D., 1981. On the crystallinity, probability of occurrence, and rheology of lava and magma.
673   Contrib. Mineral. Petrol. 78, 85–98. https://doi.org/10.1007/BF00371146

674   Métrich, N., Allard, P., Aiuppa, A., Bani, P., Bertagnini, A., Shinohara, H., Parello, F., Di Muro, A.,
675   Garaebiti, E., Belhadj, O., Massare, D., 2011. Magma and Volatile Supply to Post-collapse
676   Volcanism and Block Resurgence in Siwi Caldera (Tanna Island, Vanuatu Arc). J. Petrol. 52,
677   1077–1105. https://doi.org/10.1093/petrology/egr019

678   Michaut, C., Jaupart, C., 2011. Two models for the formation of magma reservoirs by small
679   increments. Tectonophysics 500, 34–49. https://doi.org/10.1016/j.tecto.2009.08.019

680   Michellier, C., Katoto, P. de M.C., Dramaix, M., Nemery, B., Kervyn, F., 2020. Respiratory health
681   and eruptions of the Nyiragongo and Nyamulagira volcanoes in the Democratic Republic
682   of Congo: a time-series analysis. Environ. Health 19, 62. https://doi.org/10.1186/s12940-
683   020-00615-9

684   Michon, L., Massin, F., Famin, V., Ferrazzini, V., Roult, G., 2011. Basaltic calderas: Collapse
685   dynamics, edifice deformation, and variations of magma withdrawal. J. Geophys. Res.
686   116, B03209. https://doi.org/10.1029/2010JB007636

687   Moore, C., Wright, T., Hooper, A., Biggs, J., 2019. The 2017 Eruption of Erta 'Ale Volcano, Ethiopia:
688   Insights Into the Shallow Axial Plumbing System of an Incipient Mid-Ocean Ridge.
689   Geochem.   Geophys.   Geosystems   20,   5727–5743.
690   https://doi.org/10.1029/2019GC008692

691   Morrison, A., Whittington, A., Smets, B., Kervyn, M., Sehlke, A., 2020. The rheology of crystallizing
692   basaltic lavas from Nyiragongo and Nyamuragira volcanoes, D.R.C. Volcanica 3, 1–28.
693   https://doi.org/10.30909/vol.03.01.0128

694   Naslund, H.R., McBirney, A.R., 1996. Mechanisms of Formation of Igneous Layering, in: Cawthorn,
695   R.G. (Ed.), Developments in Petrology. Elsevier, pp. 1–43. https://doi.org/10.1016/S0167-
696   2894(96)80003-0

697   Neal, C.A., Brantley, S.R., Antolik, L., Babb, J.L., Burgess, M., Calles, K., Cappos, M., Chang, J.C.,
698   Conway, S., Desmither, L., Dotray, P., Elias, T., Fukunaga, P., Fuke, S., Johanson, I.A.,
699   Kamibayashi, K., Kauahikaua, J., Lee, R.L., Pekalib, S., Miklius, A., Million, W., Moniz, C.J.,
700   Nadeau, P.A., Okubo, P., Parcheta, C., Patrick, M.R., Shiro, B., Swanson, D.A., Tollett, W.,
701   Trusdell, F., Younger, E.F., Zoeller, M.H., Montgomery-Brown, E.K., Anderson, K.R.,
702   Poland, M.P., Ball, J.L., Bard, J., Coombs, M., Dietterich, H.R., Kern, C., Thelen, W.A.,
703   Cervelli, P.F., Orr, T., Houghton, B.F., Gansecki, C., Hazlett, R., Lundgren, P., Diefenbach,
704   A.K., Lerner, A.H., Waite, G., Kelly, P., Clor, L., Werner, C., Mulliken, K., Fisher, G., Damby,
705   D., 2019. The 2018 rift eruption and summit collapse of Kīlauea Volcano. Science 363,
706   367–374. https://doi.org/10.1126/science.aav7046

707   Nicholson, R., 1994. Structural Geology by R. J. Twiss and E. M. Moores. W. H. Freeman & Co., San
708   Francisco, 1992. No. of pages: 532. Price: $47.95 (hardback). ISBN 0 7167 2252 6 . Geol. J.
709   29, 382–383. https://doi.org/10.1002/gj.3350290408

710   Patrick, M., Swanson, D., Orr, T., 2019. A review of controls on lava lake level: insights from
711   Halemaʻumaʻu   Crater,   Kīlauea   Volcano.   Bull.   Volcanol.   81,   13.
712   https://doi.org/10.1007/s00445-019-1268-y

713   Pouclet, A., 1975. Activités du volcan Nyamuragira (Rift ouest de l'Afrique Centrale), évaluation
714   des   volumes   de   matériaux   émis.   Bull.   Volcanol.   39,   466–478.
715   https://doi.org/10.1007/BF02597267

716 Pouclet, A., Bram, K., 2021. Nyiragongo and Nyamuragira: a review of volcanic activity in the Kivu
717   rift, western branch of the East African Rift System. Bull. Volcanol. 83, 10.
718   https://doi.org/10.1007/s00445-021-01435-6

719 R. Hoier, 1939. Contribution à l'étude de la morphologie du volcan Nyamuragira. Exploration du
720   Parc National Albert: Institut des parcs nationaux du Congo Belge.

721 Roche, O., Druitt, T.H., 2001. Onset of caldera collapse during ignimbrite eruptions. Earth Planet.
722   Sci. Lett. 191, 191–202. https://doi.org/10.1016/S0012-821X(01)00428-9

723 Roche, O., Druitt, T.H., Merle, O., 2000. Experimental study of caldera formation. J. Geophys. Res.
724   Solid Earth 105, 395–416. https://doi.org/10.1029/1999JB900298

725 Schultz, R.A., 1995. Limits on strength and deformation properties of jointed basaltic rock masses.
726   Rock Mech. Rock Eng. 28, 1–15. https://doi.org/10.1007/BF01024770

727 Shelly, D.R., Thelen, W.A., 2019. Anatomy of a Caldera Collapse: Kīlauea 2018 Summit Seismicity
728   Sequence in High Resolution. Geophys. Res. Lett. 46, 14395–14403.
729   https://doi.org/10.1029/2019GL085636

730 Simakin, A.G., Trubitsyn, V.P., 1995. Structural evolution of a cooling magma chamber. Izv. Phys.
731   SOLID EARTH CC Fiz. ZEMLI-Ross. Akad. NAUK 31, 132–144.

732 Smets, B., D'Oreye, N., Kervyn, F., 2014. Toward Another Lava Lake in the Virunga Volcanic Field?
733   Eos Trans. Am. Geophys. Union 95, 377–378. https://doi.org/10.1002/2014EO420001

734 Smets, B., Kervyn, M., d'Oreye, N., Kervyn, F., 2015. Spatio-temporal dynamics of eruptions in a
735   youthful extensional setting: Insights from Nyamulagira Volcano (D.R. Congo), in the
736   western branch of the East African Rift. Earth-Sci. Rev. 150, 305–328.
737   https://doi.org/10.1016/j.earscirev.2015.08.008

738 Smith, G.D., Smith, G.D., Smith, S., Gordon Dennis, 1985. Numerical Solution of Partial Differential
739   Equations: Finite Difference Methods. Clarendon Press.

740 Smith, R.L., Bailey, R.A., 1968. Resurgent Cauldrons, in: Geological Society of America Memoirs.
741   Geological Society of America, pp. 613–662. https://doi.org/10.1130/MEM116-p613

742 Sparks, R.S.J., Annen, C., Blundy, J.D., Cashman, K.V., Rust, A.C., Jackson, M.D., 2019. Formation
743   and dynamics of magma reservoirs. Philos. Trans. R. Soc. Math. Phys. Eng. Sci. 377,
744   20180019. https://doi.org/10.1098/rsta.2018.0019

745 Sparks, R.S.J., Huppert, H.E., 1984. Density changes during the fractional crystallization of basaltic
746   magmas: fluid dynamic implications. Contrib. Mineral. Petrol. 85, 300–309.
747   https://doi.org/10.1007/BF00378108

748 Swanson, D.A., Duffield, W.A., Jackson, D.B., Peterson, D.W., 1979. Chronological narrative of the
749   1969-71 Mauna Ulu eruption of Kilauea Volcano, Hawaii (Report No. 1056), Professional
750   Paper. https://doi.org/10.3133/pp1056

751 Tedesco, D., Vaselli, O., Papale, P., Carn, S.A., Voltaggio, M., Sawyer, G.M., Durieux, J., Kasereka,
752   M., Tassi, F., 2007. January 2002 volcano-tectonic eruption of Nyiragongo volcano,
753   Democratic Republic of Congo. J. Geophys. Res. 112, B09202.
754   https://doi.org/10.1029/2006JB004762

755 Ukawa, M., Fujita, E., Ueda, H., Kumagai, T., Nakajima, H., Morita, H., 2006. Long-term geodetic
756   measurements of large scale deformation at Iwo-jima caldera, Japan. J. Volcanol.
757   Geotherm. Res. 150, 98–118. https://doi.org/10.1016/j.jvolgeores.2005.07.008

758 Valade, S., Ley, A., Massimetti, F., D'Hondt, O., Laiolo, M., Coppola, D., Loibl, D., Hellwich, O.,
759   Walter, T.R., 2019. Towards Global Volcano Monitoring Using Multisensor Sentinel
760   Missions and Artificial Intelligence: The MOUNTS Monitoring System. Remote Sens. 11,
761   1528. https://doi.org/10.3390/rs11131528

762 Valade, S., Ripepe, M., Giuffrida, G., Karume, K., Tedesco, D., 2018. Dynamics of Mount
763   Nyiragongo lava lake inferred from thermal imaging and infrasound array. Earth Planet.
764   Sci. Lett. 500, 192–204. https://doi.org/10.1016/j.epsl.2018.08.004

765 Wadge, G., Burt, L., 2011. Stress field control of eruption dynamics at a rift volcano: Nyamuragira,
766   D.R.Congo. J. Volcanol. Geotherm. Res. 207, 1–15.
767   https://doi.org/10.1016/j.jvolgeores.2011.06.012

768 Wadge, G., Cole, P., Stinton, A., Komorowski, J.-C., Stewart, R., Toombs, A.C., Legendre, Y., 2011.
769   Rapid topographic change measured by high-resolution satellite radar at Soufriere Hills
770   Volcano, Montserrat, 2008–2010. J. Volcanol. Geotherm. Res. 199, 142–152.
771   https://doi.org/10.1016/j.jvolgeores.2010.10.011

772 Walker, G.P.L., 1988. Three Hawaiian calderas: An origin through loading by shallow intrusions? J.
773   Geophys. Res. Solid Earth 93, 14773–14784. https://doi.org/10.1029/JB093iB12p14773

774 Wauthier, C., Cayol, V., Poland, M., Kervyn, F., d'Oreye, N., Hooper, A., Samsonov, S., Tiampo, K.,
775   Smets, B., 2013. Nyamulagira's magma plumbing system inferred from 15 years of InSAR.
776   Geol. Soc. Lond. Spec. Publ. 380, 39–65. https://doi.org/10.1144/SP380.9

777   Worster, M.G., Huppert, H.E., Sparks, R.S.J., 1993. The crystallization of lava lakes. J. Geophys. Res.
778   98, 15891. https://doi.org/10.1029/93JB01428

779   Wright, T.L., Marsh, B., 2016. Quantification of the intrusion process at Kīlauea volcano, Hawai'i.
780   J.   Volcanol.   Geotherm.   Res.   328,   34–44.
781   https://doi.org/10.1016/j.jvolgeores.2016.09.019

782   Wright, T.L., Peck, D.L., Shaw, H.R., 1976. Kilauea lava lakes: Natural laboratories for study of
783   cooling, crystallization, and differentiation of basaltic magma. Wash. DC Am. Geophys.
784   Union Geophys. Monogr. Ser. 19, 375–390. https://doi.org/10.1029/GM019p0375

785